Check for updates

Optical Performance of a Novel Two-Receiver Solar Central Tower System

Suhil Kiwan
Department of Mechanical Engineering,
Jordan University of Science and Technology,
Irbid 22110, Jordan
e-mail: kiwan@just.edu.jo

Abdel Latif Khammash
Department of Mechanical Engineering,
Jordan University of Science and Technology,
Irbid 22110, Jordan
e-mail: Awkhammash@gmail.com

A novel idea of using two receivers on the same tower in a solar tower system is introduced and investigated. The idea is to have two receivers at the same tower at different heights and sharing the same heliostat field. The pointing strategy for each heliostat is to pick the receiver that gives the maximum optical efficiency. To investigate this idea, two receivers are placed on the tower, one at the top and one at the midway up the tower. The biomimetic "spiral" distribution scheme is used to design the heliostat field, and the particle swarm optimization (PSO) method is used to obtain the optimum field shape factors. The model equations for calculating the optical field efficiency are presented and coded using the MATLAB software. The code is validated against known cases. To quantify the effect of the idea introduced in this paper, a solar field for the 50 MWth solar tower system with a single receiver is designed for Ma'an, Jordan (Ma'an enjoys high values of direct normal irradiance). It is found that the annual weighted optical efficiency for the 50 MWth plant in Ma'an for a single receiver is 67.14%, while it reaches 67.64% using the two-receiver system. Furthermore, the study shows that having two receivers on the same tower could save two heliostats and 11,000 m^2 of needed land area to obtain the same power as a single-receiver tower. The economic analysis for this 50 MWth plant shows that savings can be obtained from having an extra receiver on the same tower of the same quality as the main receiver when the specific land area exceeds 65 $/$m^2$.
[DOI: 10.1115/1.4044189]

Keywords: solar central tower, two-receiver system, biomimetic distribution, particle swarm optimization, clean energy, efficiency, renewable, simulation, solar, solar tower

1 Introduction

Concentrated solar power (CSP) with proper thermal energy storage has a good potential for electricity generation. Among the CSP technologies, solar tower system (STS) technology provides a promising solution for the conversion of solar energy into electricity or steam generation. STS is attractive because it can accommodate simple thermal energy storage, and it can operate at high temperatures up to 2000 °C [1]. However, STS cannot be considered as a well-developed technology, yet. Researchers are still investigating many aspects of the STS technology. Ashley et al. [2] optimized the aiming strategies in solar power tower plants to avoid risks associated with thermal overloading due to sharp flux gradients.

The cost of the heliostat field comprises the highest percentage of the total cost of the STS plant [3]. Therefore, optimum solar field distribution has attracted the attention of many researchers. Radially staggered pattern [4–7], biomimetic spiral pattern [5], and parallel cornfield pattern [6] are commonly used for distributiong the heliostat field. Comparisons among these fields are presented by Refs. [8] and [9]. The biomimetic spiral distribution is a promising scheme since it develops efficient fields with less land requirement. Saghafifar et al. [10] studied the implementation of nonequal heliostat field distributed using a radially staggered pattern. Their idea was to minimize the distance between heliostats by varying their size, and they redesigned the heliostat field of PS10 plant and obtained an enhancement of 0.32%. Furthermore, the land tilt angle where the heliostats field is being installed is also another factor that affects the performance of the system, and according to Kiwan and Al Hamad [11], increasing the land tilt angle will always reduce the weighted efficiency, but reduces the required area as well.

The performance of heliostat field is also known to be influenced by system location (latitude), mirror properties, distribution of heliostats, and the receiver's size, type, and location. Some researchers investigated the receiver dimensions [7]; some researchers studied the receiver configuration such as beam down configuration [12]; and others suggested adding other receivers. Carrizosa et al. [13] studied the use of three receivers at one tower installed at different heights and different azimuthal angles, but no precise results on system efficiency were mentioned in their research. Piroozmand and Boroushaki [14] suggested using two receivers, each at a separate tower with a shared heliostat field. They obtained an enhancement of 0.26% in the optical efficiency compared with a single tower with a single receiver.

In this paper, an additional novel idea is added to the attempts for improving the solar tower system. The concept of using more than one receiver on the same tower, same azimuthal angle, and same heliostat field is presented and discussed. According to the authors' knowledge, this idea has never been addressed in the literature.

2 Modeling

The instantaneous optical efficiency of a single heliostat in a heliostat field is a function of cosine efficiency $\eta_{\cos}$, attenuation efficiency η_{att}, interception efficiency η_{int}, shading and blocking efficiency $\eta_{sh\&b}$, and mirror reflectivity η_r. It can be determined as follows:

$$\eta_h = \eta_{\cos} * \eta_{att} * \eta_r * \eta_{int} * \eta_{sh\&b} \tag{1}$$

The annual performance of a heliostat field can be expressed as annual unweighted efficiency η_{h_uw} or annual weighted efficiency η_{h_w}:

$$\eta_{h\_uw} = \frac{\sum_{n=1}^{365} \int_{sunrise}^{sunset} \eta_h(t)dt}{\sum_{n=1}^{365} \int_{sunrise}^{sunset} dt} \tag{2}$$

Contributed by the Solar Energy Division of ASME for publication in the JOURNAL OF SOLAR ENERGY ENGINEERING: INCLUDING WIND ENERGY AND BUILDING ENERGY CONSERVATION. Manuscript received September 16, 2018; final manuscript received June 23, 2019; published online July 23, 2019. Assoc. Editor: Marc Röger.

 Copyright © 2019 by ASME

Downloaded from http://micronanomanufacturing.asmedigitalcollection.asme.org/solarenergyengineering/article-pdf/142/1/011005/6422839/sol_142_1_011005.pdf by guest on 08 August 2024

$$\eta_{h\_w} = \frac{\sum_{n=1}^{365} \int_{sunrise}^{sunset} \eta_h(t) I_B(t) dt}{\sum_{n=1}^{365} \int_{sunrise}^{sunset} I_B(t) dt} \quad (3)$$

Instead of integrating Eq. (2) or (3) for 1 year, which consumes a long computational time, the procedure suggested in Refs. [14–16] is adapted here in which the 21st of each month is considered as a typical day of the month. These days are simulated with a step of 1 h from sunrise to sunset, such that the solar noon represents the middle of the studied interval.

The solar direct beam radiation used by Cruz et al. [17] is adapted here:

$$I_B = 1.353 * \left[(1 - 0.14Alt) * 0.7^{AM^{0.678}} + 0.14Alt \right] \left(\frac{kW}{m^2} \right) \quad (4)$$

where Alt is the location altitude above the sea level measured in kilometers. The air mass is calculated using the following equation:

$$AM = \frac{1}{\sin \alpha_s + 0.50572(6.07995 + \alpha_s)^{-1.6364}} \quad (5)$$

where α_s is the solar altitude measured in degrees.

The details of model equations that describes the terms used in Eqs. (2) and (3) can be found in Ref. [18]. However, within the following part of this paper, a summery list of the model equations is provided.

The cosine efficiency is a function of the incident angle θ_h, and it is given by

$$\eta_{cos} = \cos \theta_h \quad (6)$$

The mirror reflectivity, η_r, is taken as a constant value for all heliostats in the field.

The atmospheric attenuation efficiency η_{att} is calculated by assuming clear sky conditions. The common model equation for atmospheric attention [5,14,19–21] is used as follows:

$$\eta_{att} = \begin{cases} 0.99321 - 0.0001176\,SLR + 1.97*10^{-8}*SLR^2, & SLR \le 1000\,m \\ \exp(-0.0001106\,SLR), & SLR > 1000\,m \end{cases} \quad (7)$$

where SLR is the distance between the center of the heliostat and the receiver (i.e., the slant range).

The interception factor or spillage losses η_{int} is calculated according to the HFLCAL model where the flux interception factor is [22] calculated as follows:

$$\eta_{int} = \frac{1}{2\pi\sigma_{tot}^2} \int_{y_{min}}^{y_{max}} \int_{X_{min}}^{x_{max}} \exp\left(-\frac{(x - x_t)^2 + (y - y_t)^2}{2\sigma_{tot}^2} \right) dxdy \quad (8)$$

where σ_{tot} is the total dispersion of flux distribution and (x_t, y_t) is the target point of the heliostat on the receiver. The integration limits are the boundaries of the receiver aperture in the x and y local coordinates. The origin point of this coordinate is at the receiver center, and its z-axis is in the direction of the normal to the receiver [22–25]. The value of the double integration is evaluated using Riemann sums [26], where both x and y domains are divided into 20 steps at least.

The value of σ_{tot} is estimated [24,25,27] as follows:

$$\sigma_{tot} = \frac{\sqrt{SLR^2(\sigma_{Sun}^2 + \sigma_{bq}^2 + \sigma_P^2 + \sigma_{ast}^2)}}{\sqrt{\cos \theta_{rec}}} \quad (9)$$

where σ_{Sun}, σ_P, σ_{bq}, and σ_{ast} are the standard deviations of Sun shape error, pointing error, beam quality, and astigmatic aberration factor, respectively. The values of σ_{Sun}, σ_P, and σ_{bq} can be considered as constants, while the value of σ_{Sun} depends on the location. σ_P depends on tracking motors efficiency and wind loads. σ_{bq} depends on the reflectors slope errors σ_{sl} [28].

$$\sigma_{bq} = 2\sigma_{sl} \quad (10)$$

The astigmatic aberration σ_{ast} factor depends on the optical performance of the mirror, which is associated with the mirror focal distance and the radiation incident angle to the heliostat θ_h, in addition to the heliostat dimensions and location.

When determining the shading and blocking efficiency over a heliostat $\eta_{sh\&b}$, the suspected shading and blocking sources are determined using the modified range method presented by Ref. [18]. Afterward, the intersection between the heliostat plane and the vector from the Sun that passes through the suspected shading source edges is determined. This will lead to show the shading polygon on the heliostat plane. Similarly, the intersection between the heliostat plane and the target vector $\vec{T}$ that passes through the blocking source edges is determined. Then according to a polygon clipping algorithm, the active area of a heliostat is determined. Further details about finding the shading and blocking efficiency can be found in Ref. [29].

3 Heliostat Field Distribution

The coordinates of the center of each heliostat in the pattern distribution for the heliostat field are described mathematically as follows:

$$x_h = ai^b \sin(2\pi\varphi^{-2} i) \quad (11)$$

$$y_h = -ai^b \cos(2\pi\varphi^{-2} i) \quad (12)$$

where "a" and "b" are the shape factors. Typical values for a and b presented in the literature [5] are within the ranges (2, 8) and (0.5, 0.7), respectively. i is the number of the heliostat, and φ is the golden ratio, which is $\frac{1+\sqrt{5}}{2}$. The values of a and b are determined via an optimization process as will be described in subsequent sections.

3.1 Field Design Layout Restrictions.

The design of a solar field starts by distributing a large number of heliostats based on the distribution scheme, here, the Biomimetic pattern. In this study, five times the expected numbers of needed heliostats are considered. The expected number of heliostats is roughly estimated based on the number of heliostats that are needed to accomplish the design power (i.e., 50 MWth in this case) at the design time of March 21 at noon. Then, the elimination process of heliostats begins. It starts by eliminating all heliostats that did not satisfy the layout constraints: collision prevention and the initial distance between heliostats and tower. Then, all efficiencies, except shading and blocking efficiency (since it is a time-consuming process) for each heliostat at the design time, are estimated. Furthermore, to include the receiver acceptance angle constraint, virtual transmissivity is obtained from Fig. 1. Then, the optical efficiency for each heliostat is calculated, and less-efficient heliostats are progressively eliminated until the output power of the field at the design time equals the required plant capacity. Information about how to apply these restrictions can be found in Ref. [18].

3.2 Optimum Field Shape Factors.

As mentioned earlier, two variables control the dimensions of the heliostat field in the biomimetic spiral distribution scheme, namely "a" and "b." The value of each variable is obtained via an optimization process for the objective function of maximizing field annual weighted efficiency. To optimize $\eta_{h\_w}(a, b)$ based on the particle swarm optimization (PSO) algorithm, a swarm of particles is assumed in the feasible domain of decision variables (a and b). Each particle moves within the given domain of the variables and reads the output of the function with every step. The optimum output for each particle,

Downloaded from http://micronanomanufacturing.asmedigitalcollection.asme.org/solarenergyengineering/article-pdf/142/1/011005/6422839/sol_142_1_011005.pdf by guest on 08 August 2024

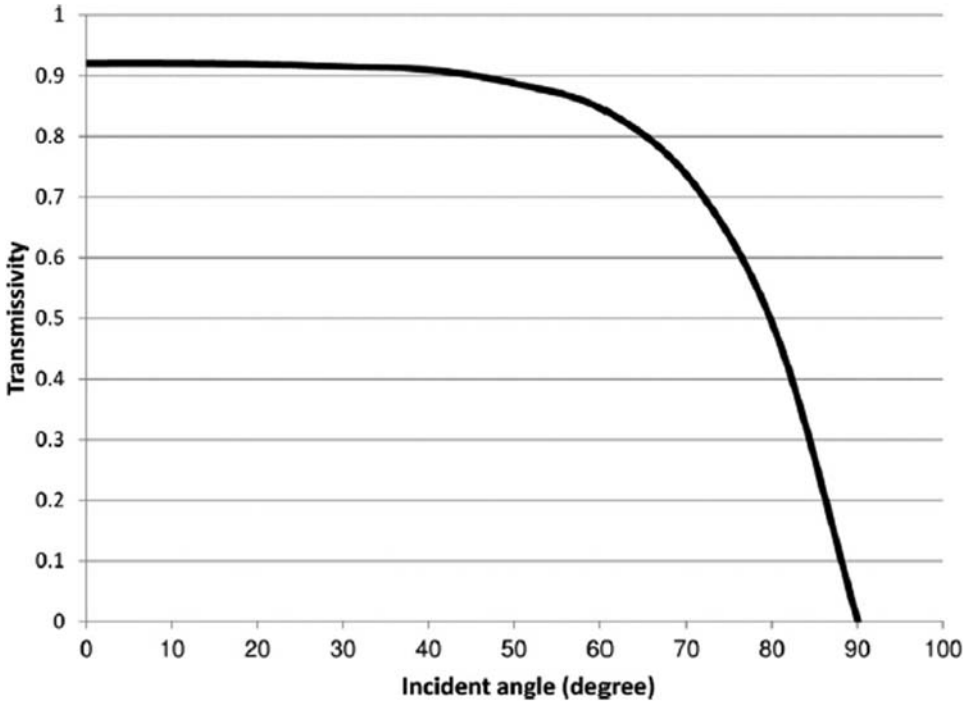

Fig. 1 Transmissivity as a function of receiver incident angle [25]

as well as the global optimum of all particles, is saved. Movement of particles continues until either the upper limit of iterations is reached or the solution converges [30,31].

The direction and magnitude of the movement of each particle are influenced by three vectors: (1) the vector of its previous movement, (2) a vector from the particle position to its own optimum position, and (3) a vector to the optimum global position of all particles as demonstrated in Fig. 2. Mathematically, this is done by using Eq. (13):

$$Q_i^{it+1} = Q_i^{it} + V_i^{it+1} \tag{13}$$

where Q is the particle position, $Q = \begin{bmatrix} a \\ b \end{bmatrix}$, the subscript i is used to indicate the number of the particle in the swarm, and "*it*" is used to indicate the iteration number. V_i is the velocity of the particle i, $V = \begin{bmatrix} V_a \\ V_b \end{bmatrix}$, and its value can be found according to the following equation:

$$V_i^{it+1} = wV_i^{it} + c_1\ \text{rand}_1(Q_{ibest}^{it} - Q_i^{it}) + c_2\ \text{rand}_2(Q_{G.\ best}^{it} - Q_i^{it}) \tag{14}$$

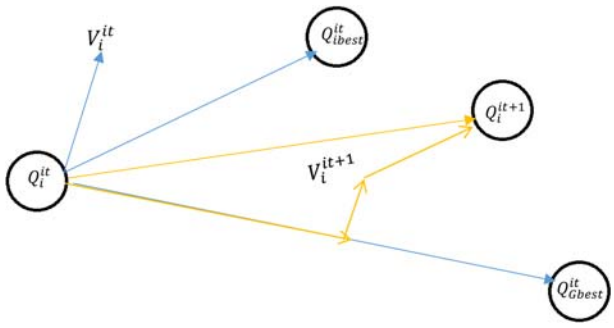

Fig. 2 Updating the PSO particle position

where w is the inertia weight and its value $w = 0.5(1 + \text{rand}_3)$, c_1 and c_2 are acceleration constants taken to be 1.6 [14], and rand_1, rand_2, and rand_3 are random numbers between 0 and 1.

To ensure a proper sweep of variables domains, upper and lower limits to the particle velocity are set. The values of these limits are [30] as follows:

$$V_{limit} = \pm 0.2(Q_{max} - Q_{min}) \tag{15}$$

In this study, a swarm of 30 particles is used, and the upper limit of iterations is set to 1000, while the convergence criteria are [14] as follows:

$$|Q_{G\ best}^{it} - Q_{G\ best}^{it-15}| < 10^{-6}\ \textit{and}\ it > 20$$

Once the solution is converged, the heliostat field area is estimated by determining the area of the convex hull that contains all the heliostats in the field. All of the equations and procedure outlined above are solved by a MATLAB code written for this purpose.

3.4 Aiming Strategy and Efficiency for the Two-Receiver System. In the two-receiver system considered in this study, each heliostat has the option to aim at any receiver. However, when a heliostat changes its aiming point, all of its efficiencies change. Moreover, the shading and blocking efficiency for surrounding heliostats are also affected. The main idea is that the heliostat's aiming point should be selected based on maximizing the annual efficiency of the field. To achieve this goal, the flowchart shown in Fig. 3 is constructed and followed. It should be noted that the aiming criterion must be followed at each time step during the iteration process in the optimization scheme and for all heliostats. It can be summarized as follows:

(1) For each heliostat, mark the neighboring heliostats that their shading and blocking efficiency could be effected at any time (i.e., heliostats within the range R_{sh}, and R_b as explained by Ref. [18]).
(2) At the starting time (i.e., beginning of the day), the heliostat's default aiming point is toward the highest receiver.
(3) Store the current decision for each heliostat.

Downloaded from http://micronanomanufacturing.asmedigitalcollection.asme.org/solarenergyengineering/article-pdf/142/1/011005/6422839/sol_142_1_011005.pdf by guest on 08 August 2024

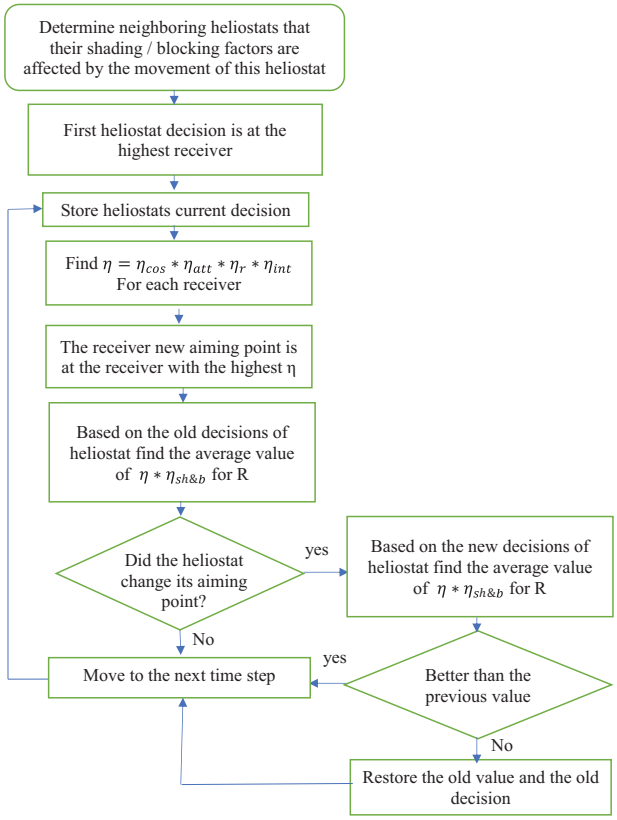

Fig. 3 Flowchart for choosing the appropriate aiming point for each heliostat

(4) Calculate the instantaneous efficiencies except for shading/blocking efficiency.
(5) Change the heliostat aiming point to another receiver and calculate its new instantaneous efficiency (without shading/blocking efficiency). Choose the receiver that gives the highest instantaneous efficiency as a target receiver. Record heliostats that changed their old decision.
(6) Assume that all heliostats are aiming at their old aiming point (i.e., early decision) and calculate the shading and blocking efficiency for all heliostats.
(7) For heliostats that changed their choice in step 5, adjust their aiming point and then study the shading and blocking factor of the heliostat itself and its corresponding group determined in step 1.
(8) Compare the efficiency of each heliostat studied in step 7 with the efficiency calculated in step 6. Choose the aiming point that produces higher overall efficiency for all heliostats determined in step 1.
(9) Repeat steps 3–9 until the day ends.

It should be noted that the algorithm developed in this paper can be considered as a modified version of Piroozmand and Boroushaki's [14] algorithm. In the algorithm developed in this paper, the heliostat changes its aiming point based on its instantaneous efficiency and the efficiency of the heliostats surrounding to it including shading and blockage efficiency. While in Piroozmand and Boroushaki algorithm, if the efficiency of the heliostat is decreased, then the algorithm will recheck the aiming point decision of all surrounding heliostats. This behavior makes the iteration time consuming.

4 Validation

The developed MATLAB code is validated against the results obtained by Piroozmand and Boroushaki [14] as well as Besarati and Goswami [25]. They used the system described in Table 1 to generate a 50 MWth power plant in Dagget, California ($\phi = 34.5$ deg N, $Alt = 610$ m). The validation was carried out at two levels. In the first level, the shape factors and number of heliostats given by each reference were taken the same without carrying out any optimization procedure. On the second level, the code starts solving the optimization problem from the beginning giving the

Table 1 System specifications and assumptions for single receiver STS system

Receiver type	Rectangular cavity	Heliostat width W_h	12.84 m
Aperture height	12 m	Heliostat height H_h	9.45 m
Aperture width	13.78 m	Slope error σ_{sl}	0 mrad
Receiver tilt angle	12.5 deg	Pointing error σ_P	2.90 mrad
Optical tower height	115 m	Sun shape error σ_{sun}	2.51 mrad
Heliostat shape	Rectangular	Field inclination	0 deg

Table 2 Comparison between solar field characteristics of Besarati and Goswami [25] using the same heliostat distribution

		Besarati and Goswami [25]	Current model
Shape factor	a	3.935	3.935
	b	0.7	0.7
Annual efficiency	η_{ref}	0.88	0.88
	η_{cos}	0.8267	0.8226
	η_{att}	0.9383	0.9401
	η_{int}	0.971	0.9713
	$\eta_{sh\&b}$	0.9698	0.9697
	η_{field_uw}	0.6446	0.6416
	η_{field_w}	0.683	0.667
Number of heliostats		594	594

Table 3 Comparison between solar field efficiencies for Dagget plant using Piroozmand and Boroushaki [14] heliostat distribution

		Piroozmand and Boroushaki [14]	Current model
Shape factor	a	3.407	3.407
	b	0.7	0.7
Annual efficiency	η_{ref}	0.88	0.88
	$\eta_{\cos}$	0.8316	0.8272
	η_{att}	0.9407	0.9452
	η_{int}	0.9865	0.9852
	$\eta_{sh\&b}$	0.9552	0.9595
	η_{field_uw}	NA	0.6504
	η_{field_w}	0.6778	0.6771
Number of heliostats		594	594

Table 4 Optimized solar field characteristics for Dagget plant using the developed code and data

		Optimization output for the developed code
Shape factor	a	3.2059
	b	0.7
Annual efficiency	η_{ref}	0.88
	$\eta_{\cos}$	0.8332
	η_{att}	0.9476
	η_{int}	0.9899
	$\eta_{sh\&b}$	0.9337
	η_{field_uw}	0.642
	η_{field_w}	0.6765

Downloaded from http://micronanomanufacturing.asmedigitalcollection.asme.org/solarenergyengineering/article-pdf/142/1/011005/6422839/sol_142_1_011005.pdf by guest on 08 August 2024

plant's capacity, ranges of shape factors a and b, and all other system and material information.

Table 2 shows a first level validation with Besarati and Goswami [25] results. It is clear that the results of the two models are very close. However, the highest deviation is registered in the field's weighted efficiency. The deviation in the weighted efficiency can be attributed to the different models of solar beam radiation used in each study. Another validation with Piroozmand and Boroushaki [14] is done, and the results are presented in Table 3. A small deviation is registered, where the difference in the weighted efficiency is less than 0.0007.

Table 5 System specifications for the four heliostats case

Receivers type	Rectangular cavity	Slope error σ_{sl}	0 mrad
Aperture height	12 m	Pointing error σ_P	2.90 mrad
Aperture width	13.78 m	Sun shape error σ_{sun}	2.51 mrad
Receivers tilt angle	12.5 deg	Latitude ϕ	34.5 deg
Receiver 1 height	130 m	Testing day	Jan. 21
Receiver 2 height	60 m	Heliostat "h_1" position	$100\vec{N}$, $40\vec{W}$
Heliostat shape	Rectangular	Heliostat "h_2" position	$600\vec{N}$, $50\vec{W}$
Heliostat height H_h	9.45 m	Heliostat "h_3" position	$200\vec{N}$, $0\vec{W}$
Heliostat width W_h	12.84 m	Heliostat "h_4" position	$626\vec{N}$, $-387\vec{W}$
Field inclination	0 deg	Height of heliostat centers	0 m

Table 6 Atmospheric attenuation for the four heliostats on different receivers

	Atmospheric attenuation factor	
Heliostat	130 m receiver	60 m receiver
h_1	0.9739	0.9790
h_2	0.9282	0.9293
h_3	0.9663	0.9695
h_4	0.9177	0.9185

A second level of validation is done by comparing all of the present model results (i.e., including the optimization results for the field shape factors) with the results of Besarati and Goswami [25]—the first column of Table 2 and the of results Piroozmand and Boroushaki [14]—the first column of Table 3. Table 4 shows the optimized results obtained by the current model. It can be noticed that the results of the unweighted efficiency of the three models are close to each other. However, it is noticed that the most significant deviation is registered within the shape factor "a" and the shading/blocking efficiency. The deviation of shading/blocking efficiency is due to the difference in the value of the range R (which is the studied range of shading and blockage sources per heliostat) used in each model. In this model, the value of R was larger than that used in other models (for details, see Ref. [18]). Other possible reasons for the deviation in the results among these models can be attributed to the difference in the solar beam radiation models, the start and end time of the simulation in each day, and the length of the time step. The runs of the simulations are conducted using Quad-Core Intel Xeon CPU (2.8 GHz, 6 GB RAM).

5 Results and Discussion

A reference case is established to investigate the effect of introducing the concepts of two receivers on the performance of STS. It is decided to design a new reference case for STS in Ma'an, Jordan. Ma'an represents a unique location since it has one of the highest values of direct normal irradiance (DNI) worldwide (2693 kW h/m^2 a) [32]. The Ma'an STS plant will serve two purposes in this paper: (1) it will be used as a reference case for comparison purposes and (2) it will represent a new STS design at this location, for possible actual installation.

5.1 Proof of Concept. To test the first concept that motivated this work, a two-receiver tower system is assumed with a field of four heliostats only. System specifications and heliostat locations are listed in Table 5. The cosine, interception, and atmospheric attenuation efficiencies for all heliostats and for each receiver are calculated and tabulated in Table 6. The detailed results are listed below:

5.1.1 Cosine Efficiency. The cosine efficiency for heliostats h_1, h_2, h_3, and h_4, are shown in Figs. 4–7, respectively. It can be

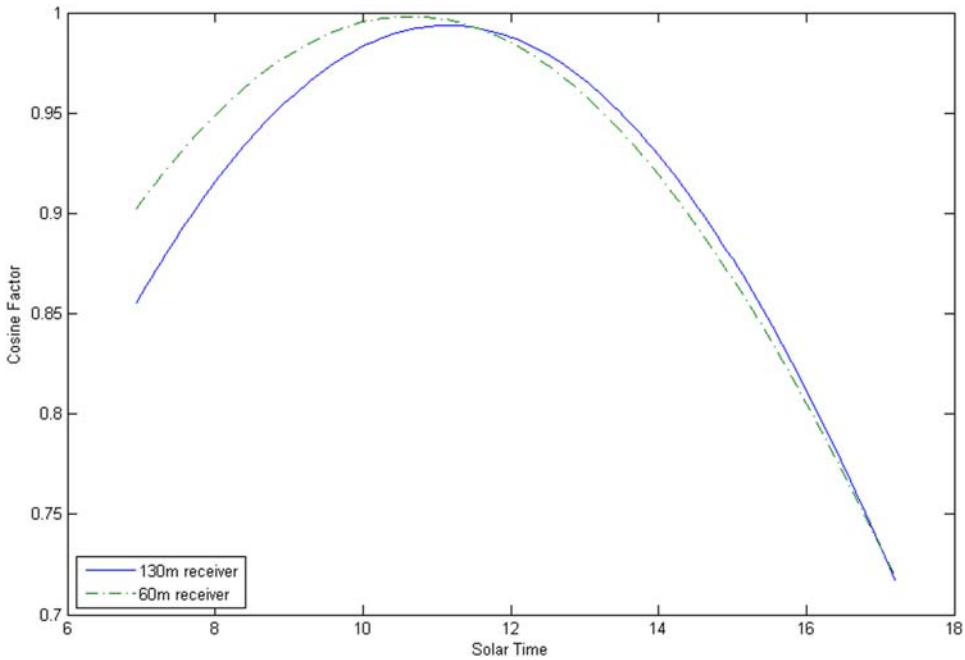

Fig. 4 Variation of cosine losses from sunrise to sunset for heliostat h_1

Downloaded from http://micronanomanufacturing.asmedigitalcollection.asme.org/solarenergyengineering/article-pdf/142/1/011005/6422839/sol_142_1_011005.pdf by guest on 08 August 2024

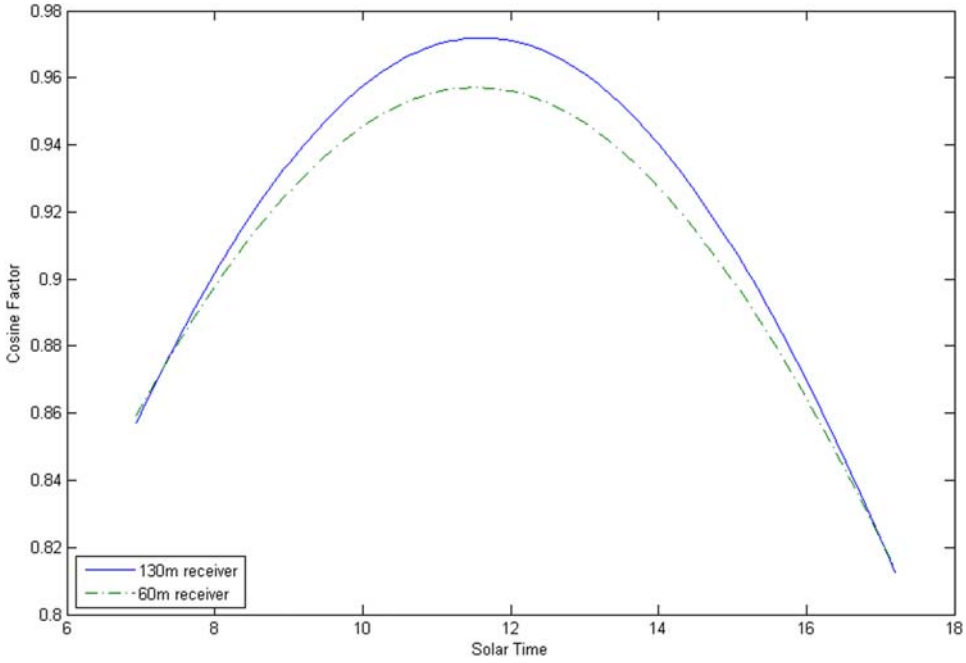

Fig. 5 Variation of cosine losses from sunrise to sunset for heliostat h_2

noticed that the cosine efficiency for heliostats h_1, h_2, and h_3 when aiming at the lower receiver at certain times is higher than that when pointing at the higher receiver. It can also be noticed that heliostats closer to the tower have higher cosine efficiency. In the given system, heliostat h_1 is the closest to the tower; thus, it benefited the most from the lower receiver. The enhancement in the cosine efficiency for this heliostat reached about 5%. However, not all heliostats benefited from the lower receivers in the same way. This is evident if the cosine efficiency of h_1 is compared with that of h_2 and h_3. It can be noticed that the enhancement was neither at the same time nor of the same value. In fact, some heliostats did not benefit from the lower receiver during the studied period as evident for heliostat h_4.

5.1.2 Interception Factor. The interception factor is affected by the cosine factor and the slant range. Both are affected by changing the receiver height. However, the study case described here shows that the interception factor for heliostats h_1 and h_3 on both receivers was recorded to be 1 for the whole day. The results for h_2 and h_4 are shown in Figs. 8 and 9, respectively. It can be noticed that both heliostats show slightly better interception factor when aiming at the lower receiver. However, more significant enhancement could be achieved for other days in the year and other heliostat locations as well.

5.1.3 Atmospheric Attenuation Factor. Atmospheric attenuation is inversely proportional to slant range. Investigation of the atmospheric attenuation factor on the given system is shown in

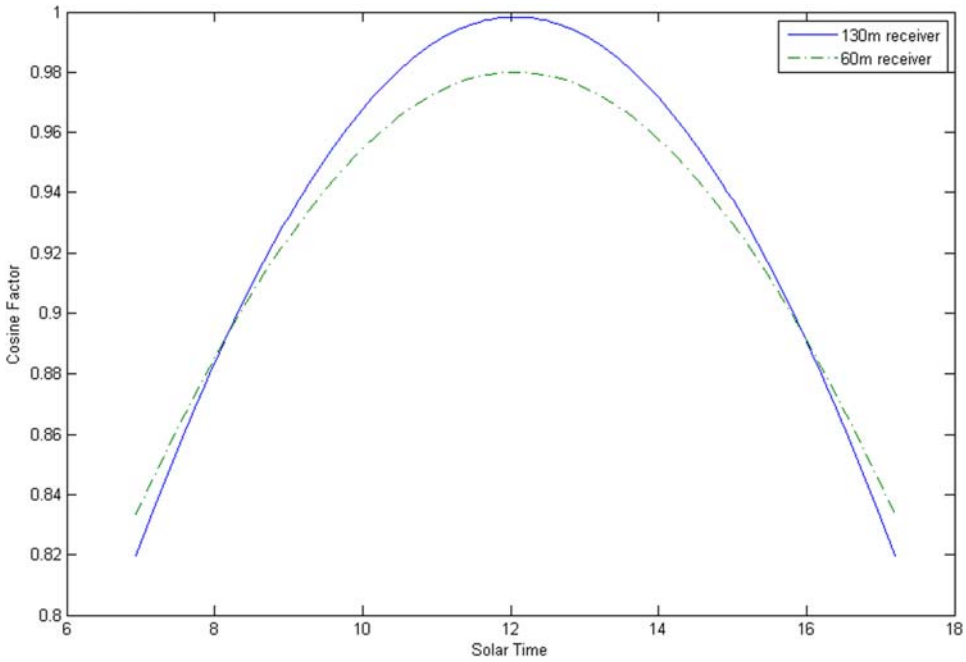

Fig. 6 Variation of cosine losses from sunrise to sunset for heliostat h_3

Downloaded from http://micronanomanufacturing.asmedigitalcollection.asme.org/solarenergyengineering/article-pdf/142/1/011005/6422839/sol_142_1_011005.pdf by guest on 08 August 2024

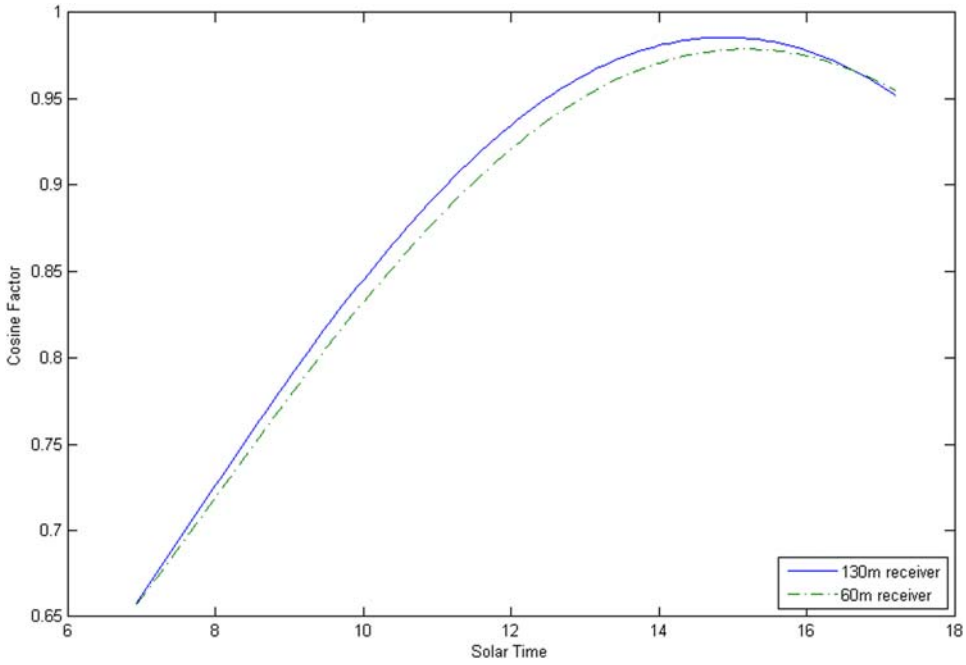

Fig. 7 Variation of cosine losses from sunrise to sunset for heliostat h_4

Table 6. It is noticed that the lower receiver produces a higher atmospheric attenuation factor.

5.2 Single-Receiver System. For the sake of developing a base point, a single-receiver system is generated in Ma'an, Jordan ($\phi = 30.18$ deg N, longitude = 35.73405 deg E, $Alt = 1100$ m). The system specifications used to generate a 50 MWth plant are shown in Table 1. The obtained field characteristics and performance are shown in Table 7, and the heliostat distribution is shown in Fig. 11. Comparing these results with a similar size plant in Dagget, California, which was generated in Table 4, it can be seen that the weighted efficiency in Ma'an's tower is less than that at Dagget by 0.51%; however, the land area needed in Ma'an's plant is less than that at Dagget's plant. This can be attributed to (1) the higher solar altitude in Ma'an and thus lower shading range per heliostat and (2) the higher DNI in Ma'an's site, which results in a reduced number of needed heliostats and thus less land for the field. The comparison also reveals that the values of both shape factors are almost equal. This slight difference in the value of $\boldsymbol{a}$ can be attributed to the difference in the latitude between the two locations (3.7 deg). To double-check these findings, the PS10 solar field has been reproduced by the current model and analyzed. The results are tabulated in Table 8. These results are obtained using the Biomimetic spiral distribution at Ma'an and at the original location of PS10. The criterion used for

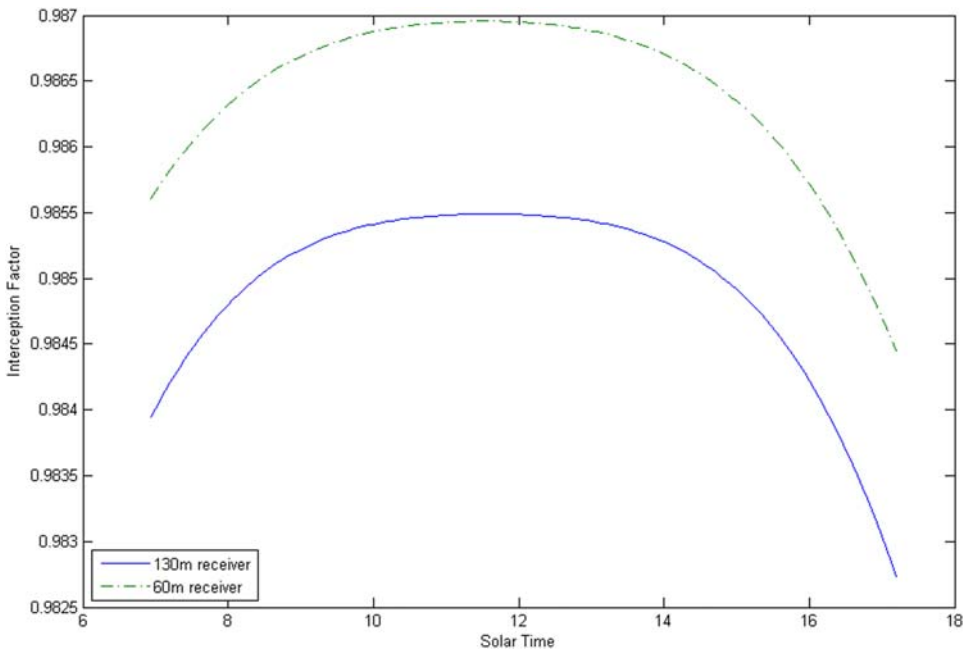

Fig. 8 Variation of the interception factor from sunrise to sunset for heliostat h_2

Downloaded from http://micronanomanufacturing.asmedigitalcollection.asme.org/solarenergyengineering/article-pdf/142/1/011005/6422839/sol_142_1_011005.pdf by guest on 08 August 2024

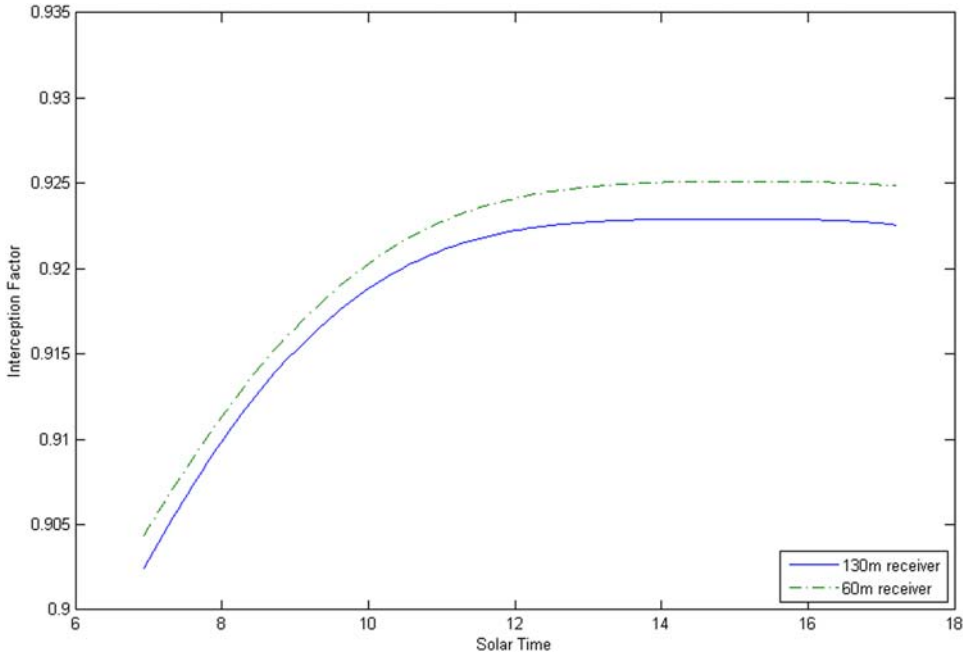

Fig. 9 Variation of the interception factor from sunrise to sunset for heliostat h_4

selecting heliostats is to choose the most efficient 624 heliostats. The results provided a similar but clearer trend to what was discussed above: about 2.8% less land area is needed in Ma'an with 4.5% higher power capacity and 1.76% less annual weighted efficiency. The difference in latitude between the two locations, in this case, is 7.26 deg. This result is consistent with the findings when comparing the plants in Dagget and Ma'an.

5.3 Two-Receiver Tower. Following the flowchart displayed in Fig. 3, a two-receiver solar field for 50 MWth with the specifications shown in Table 1 is generated in Ma'an, Jordan ($\phi = 30.18$ deg N, longitude = 35.73405 deg E, $Alt = 1100$ m). The results are listed in Table 7. Furthermore, to obtain a clear idea about the effect of having two receivers on the same tower, the field characteristics and performance for single-receiver systems located at two different heights are also calculated and added to the table. The higher receiver is at 115 m (similar to the previous case) and the lower receiver is at 60 m (almost midway to the higher receiver); see Fig. 10. The optimized heliostat distribution for all cases is presented in Figs. 11–13.

Comparing the results obtained for the heliostat distribution and performance based on the single-receiver concept at 115 m and 60 m height reveals the following: (1) The most efficient heliostats are the heliostats close to the tower, and their number in the case of the 60-m receiver is higher than that in the case of the 115 m receiver case (this is because the 0.75 H constraint is applied in both cases). (2) The number of heliostats needed for the low-receiver case is 37 more than the number required for the high-receiver case. (3) The land used in the low-receiver case is 235×10^3 m^2 higher than that in the high-receiver case (60% more). These differences are attributed to the difference in the annual efficiency for both cases. (4) The lower receiver was used with an average of 3.14% of the time by all heliostats, while heliostats located more than 300 m away aimed at the lower receiver less than 5% of the time as shown in Fig. 14.

Now, comparing these results with the results obtained for the two-receiver case, it can be noticed that a higher annual weighted efficiency is achieved in the two-receiver case (by 0.51%) compared with a single receiver at 115 m. This difference is translated to two heliostats less and 11,000 m^2 less land use. The higher efficiency came from the improvement in the cosine as well as the attention and interception efficiencies. To appreciate this efficiency enhancement, the increase in system efficiency is equivalent to the total efficiency of a solar chimney system [33,34].

It should be noted that the final decision of adapting any modification to the design of the solar field is mainly controlled by the

Table 7 Solar field performance and characteristics for cases under investigation in Ma'an, Jordan

	Variable	Single receiver 115 m	Single receiver 60 m	Two receivers 115–60 m
Shape factor	a	3.1935	3.9852	3.1721
	b	0.7	0.7	0.7
Annual efficiency	η_{ref}	0.88	0.88	0.88
	$\eta_{\cos}$	0.8292	0.8044	0.8318
	η_{att}	0.9476	0.9412	0.9498
	η_{int}	0.9902	0.9700	0.9929
	$\eta_{sh\&b}$	0.9473	0.9313	0.9448
	η_{field_uw}	0.6485	0.6035	0.6520
	η_{field_w}	0.6714	0.6180	0.6765
Field area ($\times 10^3$ m^2)		391	626	380
Number of heliostats		584	621	582

Table 8 The characteristics and performance of the solar field of PS10 plant using spiral field distribution for efficient 624 heliostats

		Spiral field at PS10 location	Ma'an
Shape factor	a	3.1920	3.1534
	b	0.7	0.6999
Annual efficiency	η_{ref}	0.88	0.88
	$\eta_{\cos}$	0.8292	0.8279
	η_{att}	0.9460	0.9466
	η_{int}	0.9869	0.9884
	$\eta_{sh\&b}$	0.9452	0.9460
	η_{field_uw}	0.6437	0.6448
	η_{field_w}	0.6797	0.6677
Field area ($\times 10^3$ m^2)		427	415
Power output (MWth)		54.06	56.49

Downloaded from http://micronanomanufacturing.asmedigitalcollection.asme.org/solarenergyengineering/article-pdf/142/1/011005/6422839/sol_142_1_011005.pdf by guest on 08 August 2024

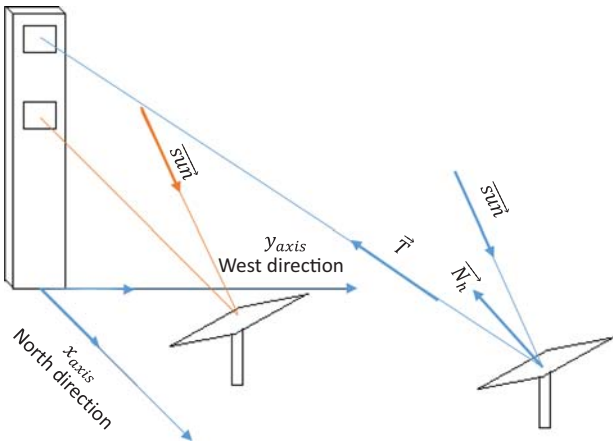

Fig. 10 The proposed two-cavity receiver tower system

system efficiency and the resulting economic merits of the system. Thus, the exact trade-off between the cost, thermal losses, and efficiency enhancements using two receivers can be determined by the designer of the complete system. This trade-off mainly depends on the size of the system, the size of each receiver, and the technology used in the power block. Thus, the use of the extra receiver (in this case the lower one) in the power block depends on the technology of producing electricity. The extra receiver can be used as a preheater or reheater in the power block or as a first-stage heater to the heat transfer fluid. Moreover, in order to obtain accurate numbers regarding the thermal losses of the proposed system, one needs to investigate a specific design and calculate the total thermal losses from the two receivers and compare it with the losses with a single receiver. One also should note that the thermal losses of the two receivers system are not necessarily much higher than that in a single receiver due to the difference in operating temperatures. In a single-receiver system, the operating temperature is high and thus the losses are high. While in the two-receiver system, the operating temperature will be lower and thus the losses are less.

6 Safe Path

The area between the upper receiver and the lower receiver on the tower is considered to be a safe path for heliostats to follow when changing their aiming point. For this area to be a safe path, it must be able to withstand the maximum total incident heat flux on it. In order to calculate the maximum incident heat flux on this area, the reflected heat flux from all heliostats that will use this path during a period of time (here we used 4 min) is calculated in two steps: first, all heliostats that will change their aiming point are identified and then the reflected power of these heliostat is determined according to the following equation:

$$\text{Power on safe path} = \sum I * A_h * \eta_h \tag{16}$$

where A_h is the area of heliostat and η_h is the instantaneous optical efficiency of the heliostat.

Results showed that the maximum solar power received by the safe path is in December. Figures 15 and 16 show the number of heliostats changing their aiming point and the reflected power on the safe path in December, respectively. It is clear that the safe path area must withstand an incident radiation of 700 kW.

7 Economic Analysis

To shed some light on the economics of using an additional receiver, a balance between the savings achieved from having two receivers on the same tower and the cost of the extra receiver should be estimated.

The savings in the case addressed in this paper come from the extra 0.5% improvements in weighted efficiency, 11,000 m^2 less land area and the two less heliostats. It has been found that the available solar energy is 3127 kW h/m^2.ann (where the available solar energy is considered whenever the solar altitude is larger than 10 deg). Assuming that electricity conversion efficiency is 30.7% [15], which is similar to the turbine used in original PS10, and the selling price of electricity is 0.15 $/kW h. Thus, simple calculation follows Eq. (17) reveals that the present value of savings results

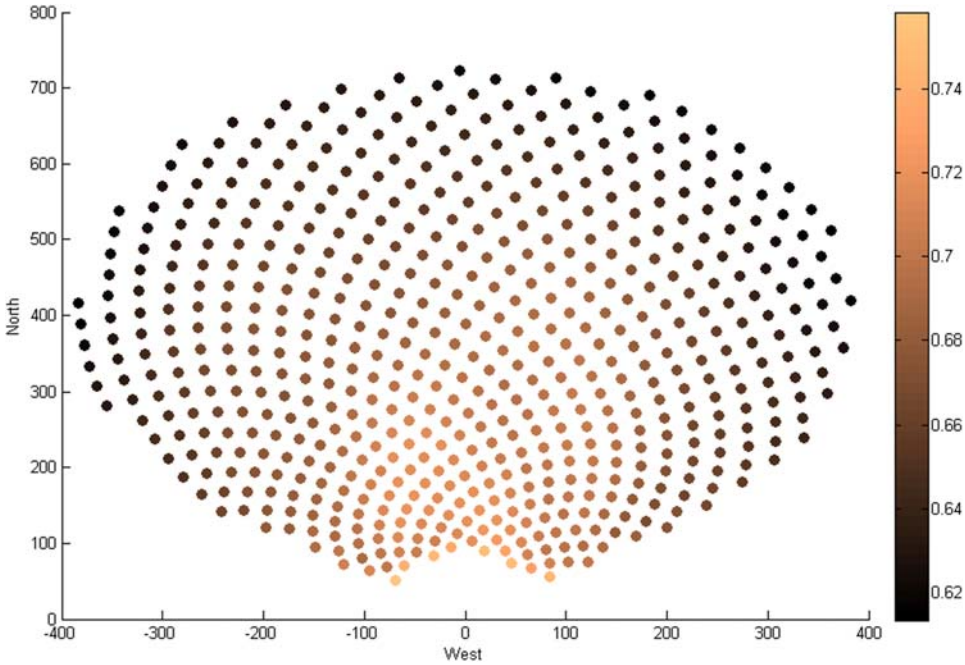

Fig. 11 Optimized solar field distribution for a single receiver in Ma'an, Jordan (receiver height, 115 m). Bar depicts the annual weighted efficiency.

Downloaded from http://micronanomanufacturing.asmedigitalcollection.asme.org/solarenergyengineering/article-pdf/142/1/011005/6422839/sol_142_1_011005.pdf by guest on 08 August 2024

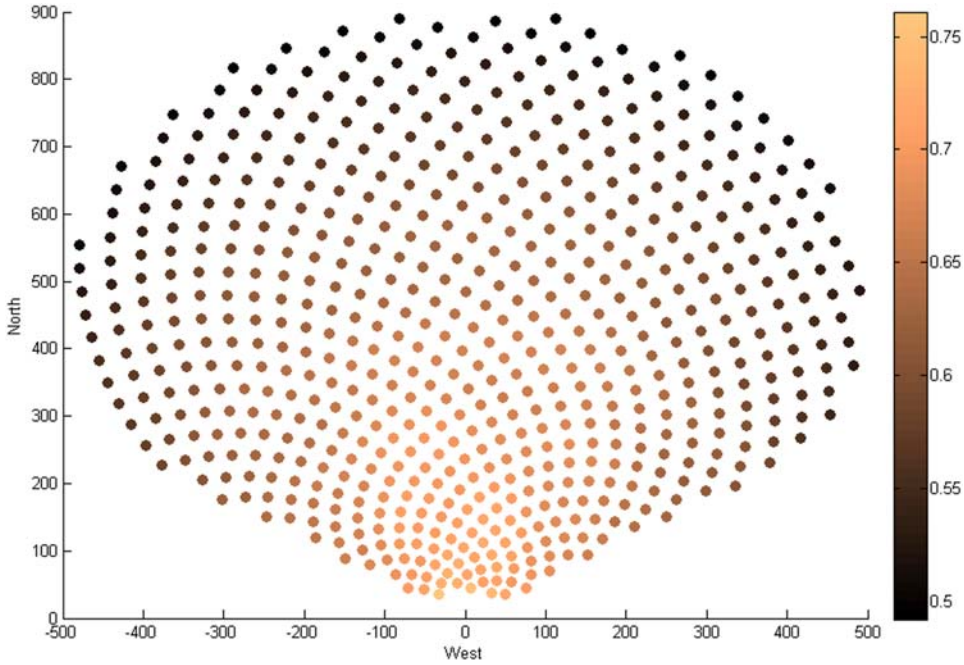

Fig. 12 Optimized solar field distribution for a single receiver in Ma'an, Jordan (receiver height, 60 m). Bar depicts the annual weighted efficiency.

from using the extra receiver "PS."

$$PS = A_h * C_h(N_{old} - N_{new}) + C_L * (A_{Lold} - A_{Lnew}) + I_{tot} * A_h * \eta_c * S * (\eta_{o\,new} * N_{new} - \eta_{o\,old} * N_{old})\left(\frac{1-(1+r)^{-n}}{r}\right) \quad (17)$$

where I_{tot} is the total received energy per square meter of heliostat per year, A_h is the area of a heliostat, η_c is the thermal to electrical conversion efficiency, S is the electricity celling price, N is the number of heliostats, and η_o is the optical efficiency. C_h is the specific cost of heliostat field including engineering, production, transport, erection, power supply and communication, and start-up tests: $C_h = 150$ \$/m^2 [35]. C_L is the specific cost of the land which could vary between 20 \$/m^2 and 100 \$/m^2.

If, for instance, we consider $C_L = 20$ \$/m^2, the life span of 25 years and the discount rate r of (8%) [36], then the total present value of the saving obtained from having two receivers is \$559, 562. The specific savings per square meter of the aperture area of the receiver considered in this study is 3384 \$/m^2. According to

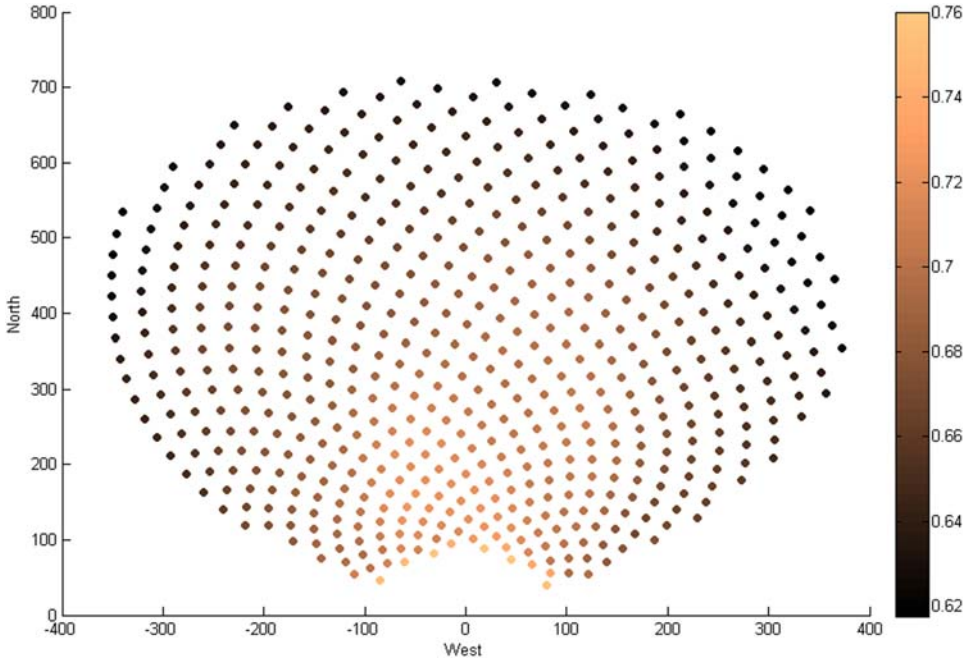

Fig. 13 Optimized solar field distribution for two receivers in Ma'an, Jordan (receiver height, 115 and 60 m). Bar depicts the annual weighted efficiency.

Downloaded from http://micronanomanufacturing.asmedigitalcollection.asme.org/solarenergyengineering/article-pdf/142/1/011005/6422839/sol_142_1_011005.pdf by guest on 08 August 2024

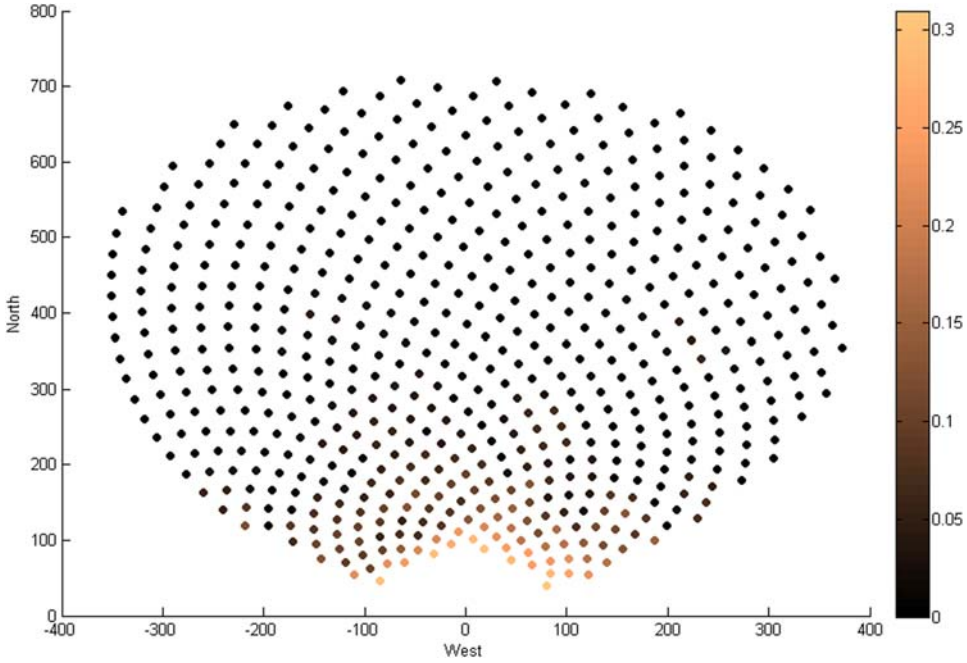

Fig. 14 The time percentage of aiming at the lower receiver per heliostat

this value, it seems that the feasibility of having two receivers on the same tower is questionable since the typical cost of a receiver per aperture area is around 6500 $/m^2. But, the secondary receiver receives less radiation than the primary receiver, and thus, its size can be reduced less than a typical main tower receiver. Thus, a decrease in the receiver cost can be achieved if the size of the secondary receiver is optimized.

If we assume that the current cost of technology is fixed and the cost of land changes from one site into another, Fig. 17 shows the variation of the present value of the specific savings per receiver aperture area with the variation of land cost. It is clear from this figure that the break-even point between the savings and the cost of having an extra receiver is achieved when the land cost increases more than 65 $/m^2.

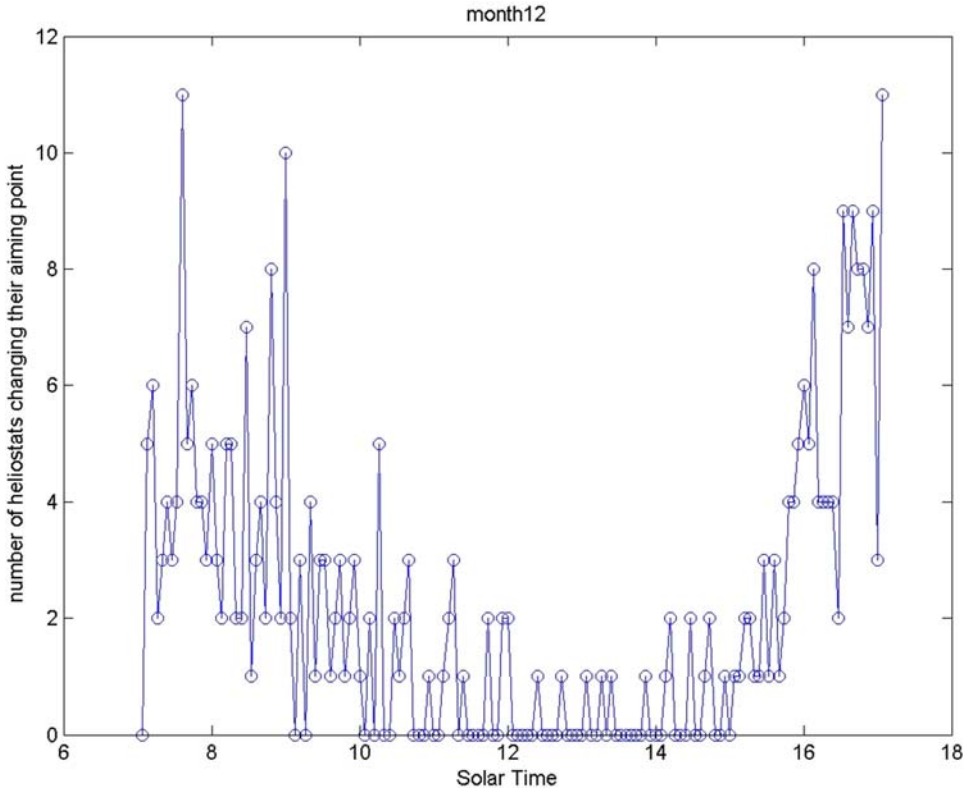

Fig. 15 Number of heliostats changed their aiming point per time step of 4 min

Downloaded from http://micronanomanufacturing.asmedigitalcollection.asme.org/solarenergyengineering/article-pdf/142/1/011005/6422839/sol_142_1_011005.pdf by guest on 08 August 2024

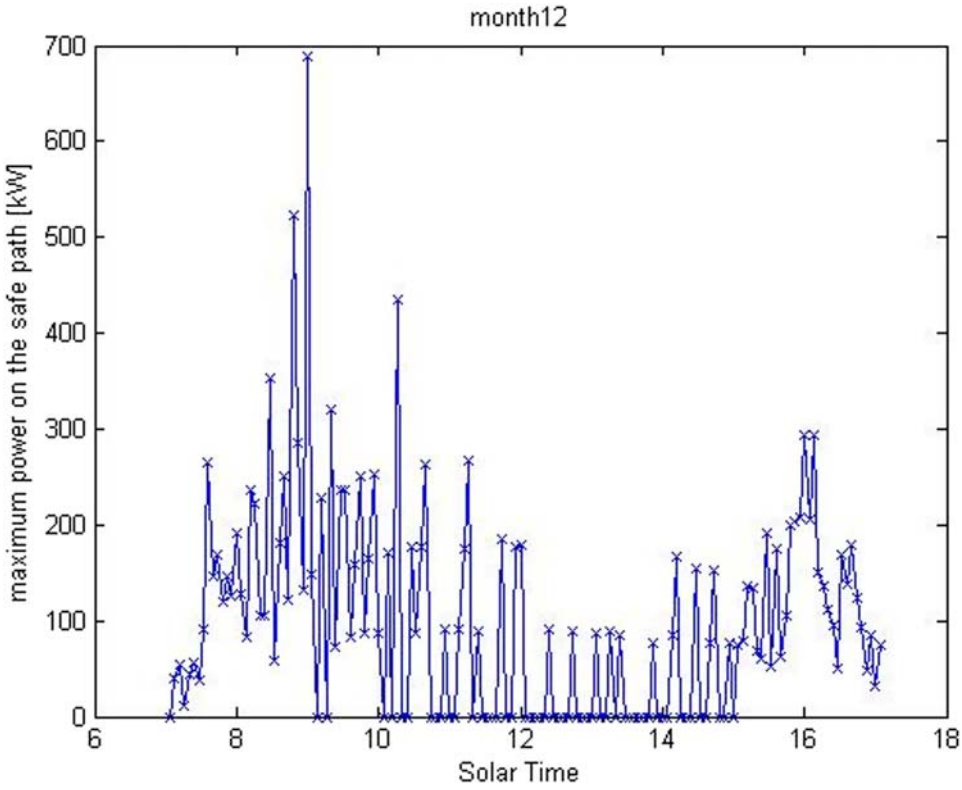

Fig. 16 Maximum possible power on the safe path

8 Conclusions

In this paper, a novel idea to improve the solar field optical efficiency in the STS system is investigated. The idea of having more than one receiver at the same tower was addressed. The use of two receivers on the same tower is simulated using the biomimetic spiral field distribution for heliostats. The PSO algorithm is used to optimize the heliostat field. A MATLAB code was developed during this work to solve the models' equations. The code was verified using known cases, and it was proved to be accurate. Furthermore, a 50 MWth STS system with a single receiver is designed in Ma'an, Jordan, and its optical performance is investigated and documented.

It is found that the annual weighted optical efficiency for a 50 MWth system design in Ma'an, Jordan, is 67.14%, which is very close to the efficiency of the plant located in Dagget, California (67.65%). Moreover, using two receivers enhances the annual weighted optical efficiency by 0.5% compared with a single-receiver model. Economic analysis under the current prices of technologies shows that having an extra receiver on the same tower is feasible when the specific cost of land is more than 65 $/m^2$.

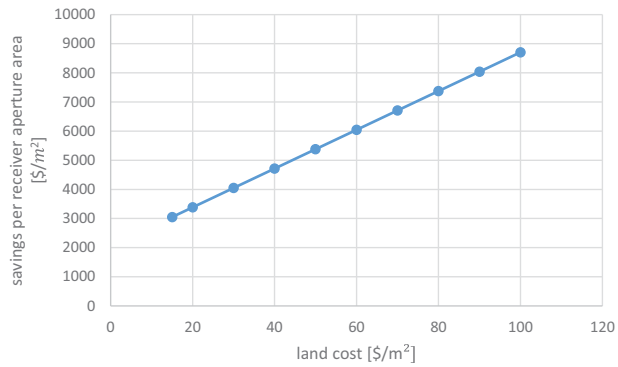

Fig. 17 The effect of land cost on the present value of savings per square meter of receiver aperture

Nomenclature

Symbols

a = the first shape factor of spiral field
b = the second shape factor of spiral field
c = acceleration constant
i = counter
r = interest rate
A = area
C = cost
H = height dimension, m
I = solar radiation, W/m^2
N = number
Q = particle position in the PSO algorithm
R = range, m
T = the vector from heliostat to the target point, m
V = particle velocity in the PSO algorithm
W = width dimension, m
Alt = altitude above sea level, km
it = iteration number
PS = present value of savings
SLR = slat range, m

Greek Symbols

ϕ = latitude angle, deg
η = efficiency
θ = incident angle, deg
σ = standard deviation
τ = transmittance
φ = golden ratio $(1 + \sqrt{5})/2$

Downloaded from http://micronanomanufacturing.asmedigitalcollection.asme.org/solarenergyengineering/article-pdf/142/1/011005/6422839/sol_142_1_011005.pdf by guest on 08 August 2024

Subscripts

- *ast* = astigmatic
- *att* = atmospheric attenuation factor
- *B* = direct beam
- cos = cosine factor
- *h* = heliostat
- *i* = counter
- *int* = interception factor
- *L* = land
- *P* = pointing
- *r* = mirror reflectivity factor
- *rec* = receiver
- *s* = sun
- *sh* = shade
- *sh&b* = shading and blocking
- *sl* = slope
- *t* = target point
- *tot* = total
- *uw* = unweighted
- *w* = weighted

References

[1] Foster, R., Ghassemi, M., and Cota, A., 2010, *Solar Energy: Renewable Energy and the Environment*, Taylor & Francis Group, New York.

[2] Ashley, T., Carrizosa, E., and Fernández-Cara, E., 2017, "Optimisation of Aiming Strategies in Solar Power Tower Plants," Energy, **137**, pp. 285–291.

[3] Emes, M. J., Arjomandi, M., and Nathan, G. J., 2015, "Effect of Heliostat Design Wind Speed on the Levelised Cost of Electricity From Concentrating Solar Thermal Power Tower Plants," Sol. Energy, **115**, pp. 441–451.

[4] Kistler, B. L., 1986, "A User's Manual for DELSOL3: A Computer Code for Calculating the Optical Performance and Optimal System Design for Solar Thermal Central Receiver Plants," p. Medium: X; Size: p. 231.

[5] Noone, C. J., Torrilhon, M., and Mitsos, A., 2012, "Heliostat Field Optimization: A New Computationally Efficient Model and Biomimetic Layout," Sol. Energy, **86**(2), pp. 792–803.

[6] Zhou, Y., and Zhao, Y., 2014, "Heliostat Field Layout Design for Solar Tower Power Plant Based on GPU," IFAC Proc. Vol., **47**(3), pp. 4953–4958.

[7] Ramos, A., and Ramos, F., 2012, "Strategies in Tower Solar Power Plant Optimization," Sol. Energy, **86**(9), pp. 2536–2548.

[8] Mutuberria, A., Pascual, J., Guisado, M. V., and Mallor, F., 2015, "Comparison of Heliostat Field Layout Design Methodologies and Impact on Power Plant Efficiency," Energy Procedia, **69**, pp. 1360–1370.

[9] Barberena, J. G., Larrayoz, A. M., Sánchez, M., and Bernardos, A., 2016, "State-of-the-Art of Heliostat Field Layout Algorithms and Their Comparison," Energy Procedia, **93**, pp. 31–38.

[10] Saghafifar, M., Gadalla, M., and Mohammadi, K., 2019, "Thermo-Economic Analysis and Optimization of Heliostat Fields Using AINEH Code: Analysis of Implementation of Non-Equal Heliostats (AINEH)," Renew. Energy, **135**, pp. 920–935.

[11] Kiwan, S., and Al Hamad, S., 2018, "On Analyzing the Optical Performance of Solar Central Tower Systems on Hillsides Using Biomimetic Spiral Distribution," ASME J. Sol. Energy Eng., **141**(1), p. 011010.

[12] Vant-Hull, L., 2014, "Issues With Beam-Down Concepts," Energy Procedia, **49**, pp. 257–264.

[13] Carrizosa, E., Domínguez-Bravo, C., Fernández-Cara, E., and Quero, M., 2015, "Optimization of Multiple Receivers Solar Power Tower Systems," Energy, **90**, pp. 2085–2093.

[14] Piroozmand, P., and Boroushaki, M., 2016, "A Computational Method for Optimal Design of the Multi-Tower Heliostat Field Considering Heliostats Interactions," Energy, **106**, pp. 240–252.

[15] Mustafa, M. A., Abdelhady, S., and Elweteedy, A. A., 2012, "Analytical Study of an Innovated Solar Power Tower (PS10) in Aswan," Int. J. Energy Eng., **2**(6), pp. 273–278.

[16] Pitz-Paal, R., Botero, N. B., and Steinfeld, A., 2011, "Heliostat Field Layout Optimization for High-Temperature Solar Thermochemical Processing," Sol. Energy, **85**(2), pp. 334–343.

[17] Cruz, N. C., Redondo, J. L., Berenguel, M., Álvarez, J. D., Becerra-Teron, A., and Ortigosa, P. M., 2017, "High Performance Computing for the Heliostat Field Layout Evaluation," J. Supercomput., **73**(1), pp. 259–276.

[18] Kiwan, S., and Khammash, A. L., 2018, "Investigations Into the Spiral Distribution of the Heliostat Field in Solar Central Tower System," Sol. Energy, **164**, pp. 25–37.

[19] Wei, X., Lu, Z., Yu, W., and Wang, Z., 2010, "A New Code for the Design and Analysis of the Heliostat Field Layout for Power Tower System," Sol. Energy, **84**(4), pp. 685–690.

[20] Ewert, M., and Fuentes, O. N., 2012, "Modelling and Simulation of a Solar Tower Power Plant," http://www.mathcces.rwthaachen.de/_media/5people/frank/solartower.pdf/, Accessed July 16, 2019.

[21] Eddhibi, F., Ben Amara, M., Balghouthi, M., and Guizani, A., 2015, "Optical Study of Solar Tower Power Plants," J. Phys. Conf. Ser., **596**(1), p. 012018.

[22] Besarati, S. M., Goswami, D. Y., and Stefanakos, E. K., 2014, "Optimal Heliostat Aiming Strategy for Uniform Distribution of Heat Flux on the Receiver of a Solar Power Tower Plant," Energy Convers. Manag., **84**, pp. 234–243.

[23] Schwarzbözl, P., Schmitz, M., and Pitz-Paal, R., 2009, "Visual HFLCAL—A Software Tool for Layout and Optimisation of Heliostat Fields," SolarPACES Conf., pp. 15–18.

[24] Collado, F. J., 2010, "One-Point Fitting of the Flux Density Produced by a Heliostat," Sol. Energy, **84**(4), pp. 673–684.

[25] Besarati, S. M., and Goswami, D. Y., 2014, "A Computationally Efficient Method for the Design of the Heliostat Field for Solar Power Tower Plant," Renew. Energy, **69**, pp. 226–232.

[26] Anton, H., Bivens, I., and Davis, S., 2009, *Calculus Early: Trancendentals*, 9th ed., Laurie Rosatone, Jefferson City.

[27] Goswami, D. Y., 2015, *Principles of Solar Engineering*, 3rd ed., Taylor & Francis Group, New York.

[28] Khammash, A. L., 2017, Using Multi-Receivers in Solar Central Tower Systems, M.Sc. thesis, Jordan University Of Science and Technology, Ramtha, Jordan.

[29] Ramos, A., and Ramos, F., 2014, "Heliostat Blocking and Shadowing Efficiency in the Video-Game Era," arXiv Prepr. arXiv1402.1690, p. 8.

[30] Marini, F., and Walczak, B., 2015, "Particle Swarm Optimization (PSO). A Tutorial," Chemom. Intell. Lab. Syst., **149**, pp. 153–165.

[31] Dash, J., Dam, B., and Swain, R., 2016, "Optimal Design of Linear Phase Multi-Band Stop Filters Using Improved Cuckoo Search Particle Swarm Optimization," Appl. Soft Comput., **52**, pp. 435–445.

[32] SOLARGIS, 2017, "Direct Solar Irradiation Map," solargis.info.

[33] Toghraie, D., Karami, A., Afrand, M., and Karimipour, A., 2018, "Effects of Geometric Parameters on the Performance of Solar Chimney Power Plants," Energy, **162**, pp. 1052–1061.

[34] Kiwan, S., Al-Nimr, M., and Abdel Salam, Q. I., 2018, "Solar Chimney Power-Water Distillation Plant (SCPWDP)," Desalination, **445**, pp. 105–114.

[35] Schmitz, M., Schwarzbozl, P., Buck, R., and Pitz-Paal, R., 2006, "Assessment of the Potential Improvement Due to Multiple Apertures in Central Receiver Systems With Secondary Concentrators," Sol. Energy, **80**, pp. 111–120.

[36] Li, C., Zhai, R., Yang, Y., Patchigolla, K., Oakey, J. E., and Turner, P., 2019, "Annual Performance Analysis and Optimization of a Solar Tower Aided Coal-Fired Power Plant," Appl. Energy, **237**, pp. 440–456.

Downloaded from http://micronanomanufacturing.asmedigitalcollection.asme.org/solarenergyengineering/article-pdf/142/1/011005/6422839/sol_142_1_011005.pdf by guest on 08 August 2024